Electronic Supplementary Material (ESI) for Journal of Materials Chemistry A.

Supporting Information

Highly Conductive Electrocatalytic Gold Nanoparticle-Assembled Carbon Fiber Electrode for High-Performance Glucose-Based Biofuel Cells†

Cheong Hoon Kwon[a], Yongmin Ko[a,b], Dongyeeb Shin[a], Seung Woo Lee*[b] and Jinhan Cho*[a]

[a]Department of Chemical and Biological Engineering, Korea University, 145 Anam-ro, Seongbuk-gu, Seoul 02841, Republic of Korea. *E-mail: jinhan71@korea.ac.kr

[b]The George W. Woodruff School of Mechanical Engineering, Georgia Institute of Technology, Atlanta, Georgia 30332, USA. *E-mail: seung.lee@me.gatech.edu.

Toxic chemical issues of Au-CF electrodes.

First, the outermost layer of the cathode (*i.e.* Au NP-coated CF electrode) was composed of ethanol-based TREN instead of toluene-based TOABr-Au NPs. Therefore, the repetitive ethanol washing steps after the adsorption of TREN can almost completely remove the residual toluene solvent within electrodes because toluene and ethanol can be well mixed (see Experimental Section). Particularly, it is well-known that ethanol is biocompatible because of its relatively high hydrogen content, availability, non-toxicity, and storage and handling safety.[1] Second, all TOABr ligands of TOABr-Au NPs were replaced and removed by the amine ($-NH_2$) groups of TREN (See **Fig. S4b**). In the case of PEI linkers, PEI has been widely used in a number of biology area related to tissue culture. Although the excess use of PEI might be weakly toxic to cells,[2] the PEI in our study has the stable and strong covalent-bonding with the Au NP-coated electrode, and resultantly the desorption of PEI from the electrodes can be minimized.

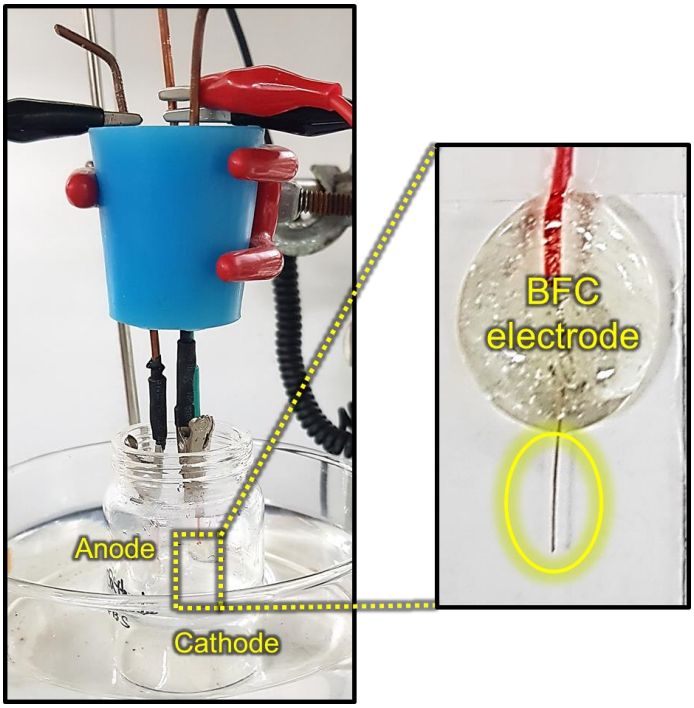

Fig. S1 The photographs of a complete Au-CF BFC. The image of 20-Au-CF BFC cathode (right).

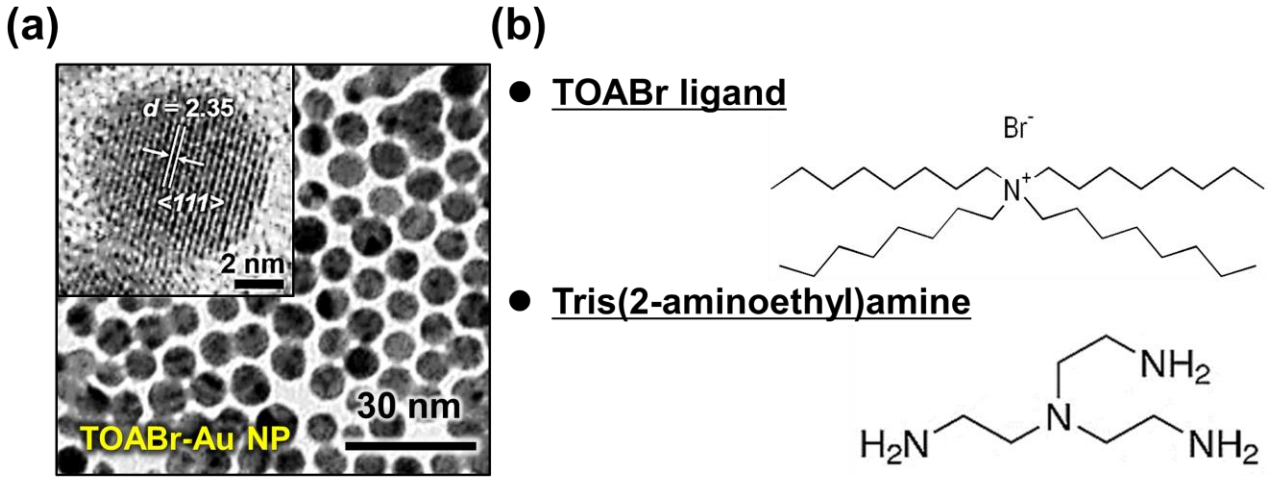

Fig. S2 (a) Transmission Electron Microscopy (TEM) image of TOABr-Au NP. Inset shows the spacing of the lattice fringe of the TOABr-Au NP (2.4 Å), which corresponds to the Au (111) crystalline planes. (b) The molecular structures of native TOABr ligand and TREN.

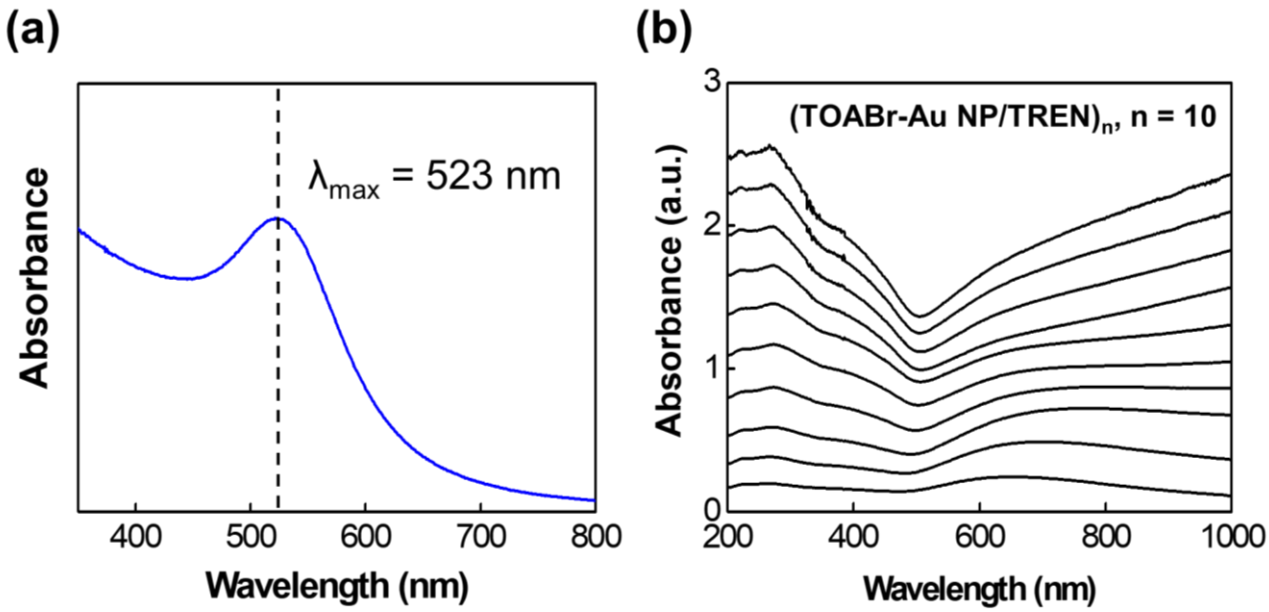

Fig. S3 (a) UV absorbance peak of TOABr-Au NP. (b) UV-vis absorbance spectra of (TOABr-Au NP/TREN)$_n$ multilayers on a quartz substrate as a function of bilayer number.

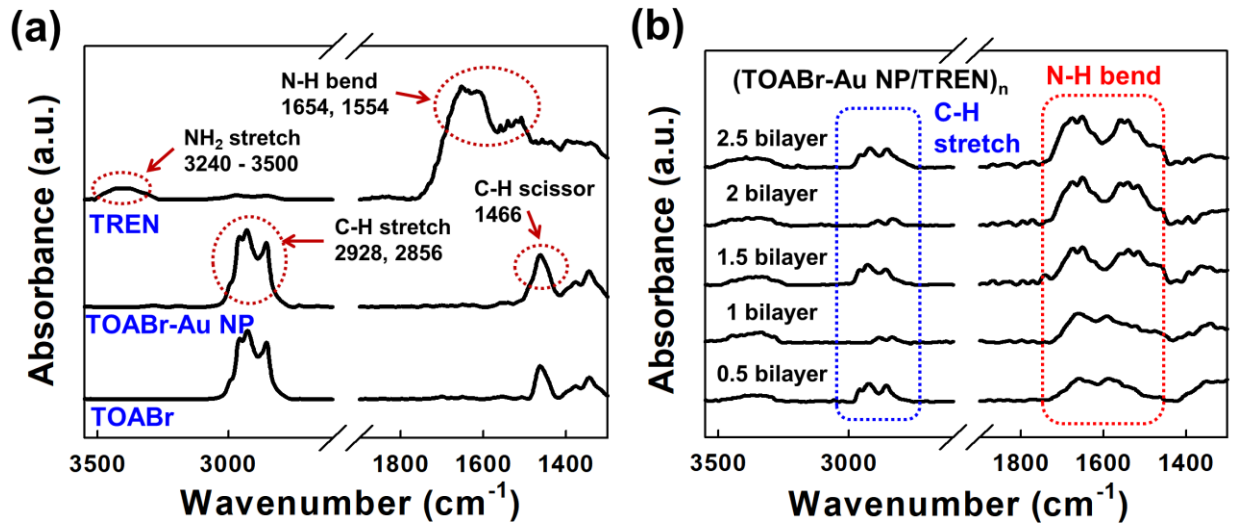

Fig. S4 (a) Fourier-transform infrared spectroscopy (FTIR) spectra of each materials (TREN, TOABr-Au NP, and TOABr). (b) FTIR spectra of TOABr-Au NP/TREN multilayer films as increasing the bilayer number on the PEI-coated substrate.

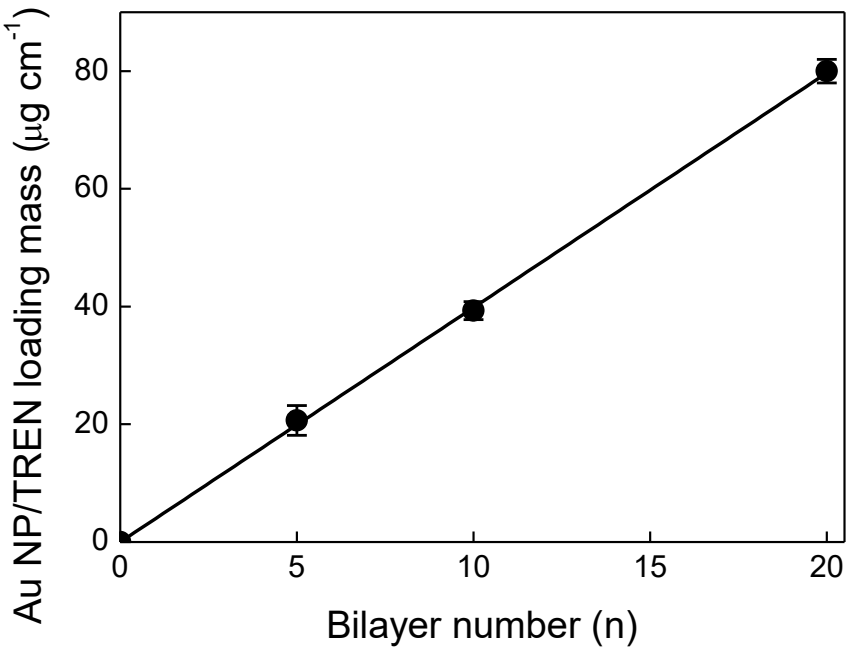

Fig. S5 Change in Au NP/TREN loading mass absorbed onto the pristine CF electrode as increasing the bilayer number (n).

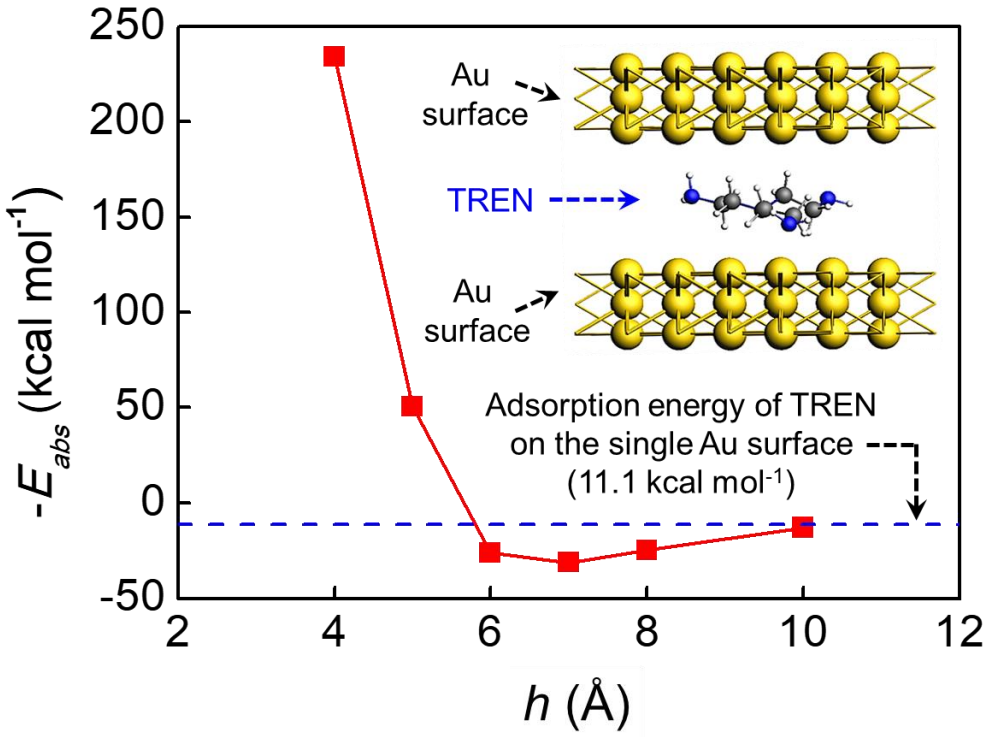

Fig. S6 DFT-computed adsorption energy (E_{abs}) of TREN linker between Au surfaces as a function of separation distance (h). The blue dashed line represents the adsorption energy of TREN on the single Au surface. Inset: Geometry-optimized molecular structure of TREN at the separation distance h = 7Å.

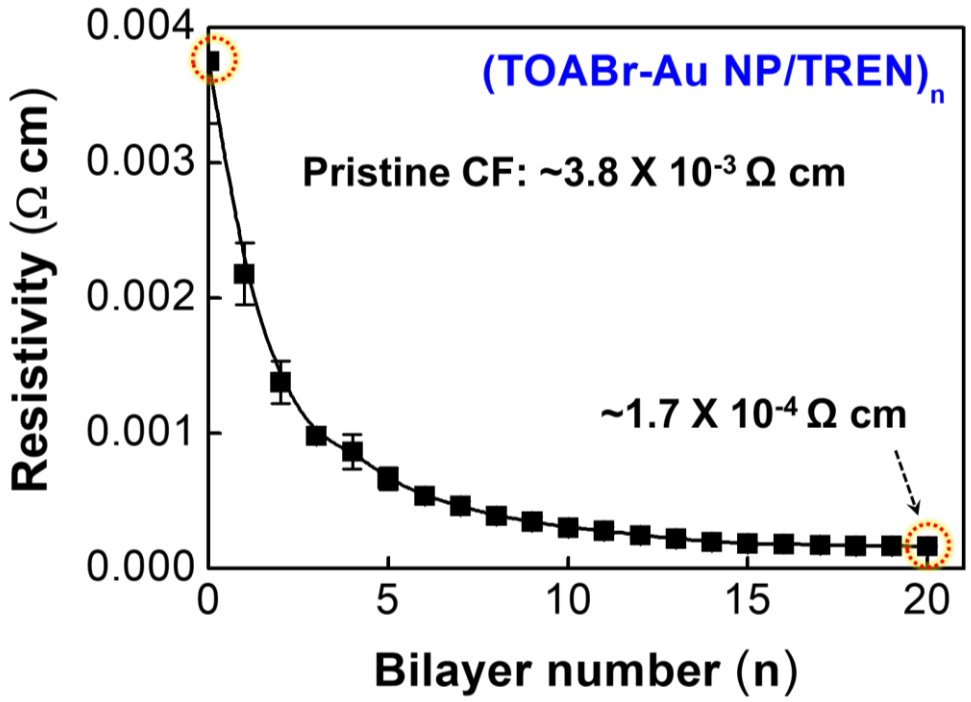

Fig. S7 Resistivity of n-Au-CF as a function of bilayer number (n).

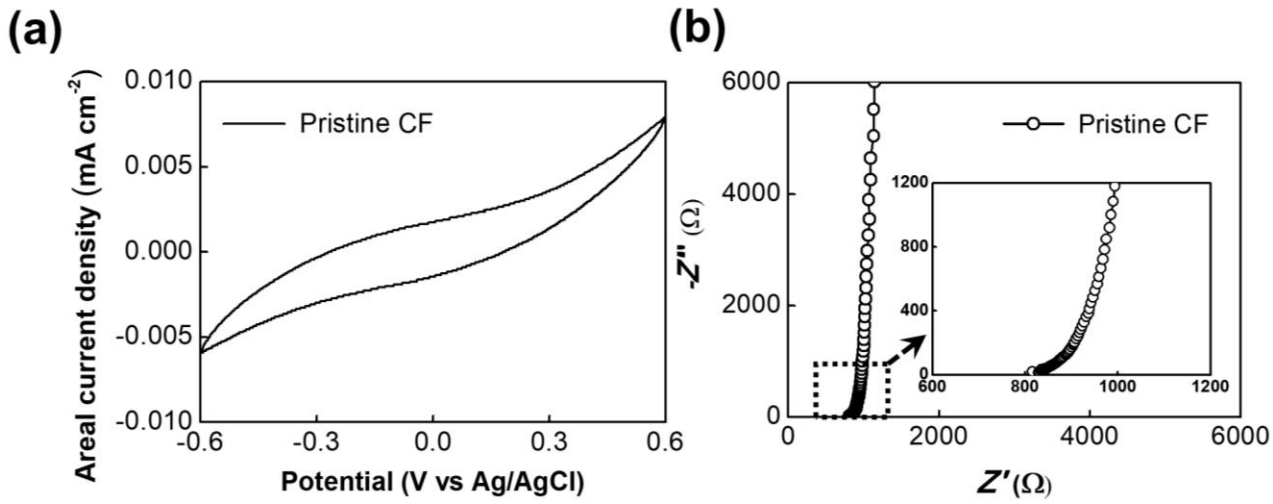

Fig. S8 Cyclic voltammetry (a) and Nyquist curve (b) of the pristine (Au NP-free) carbon fiber (CF) electrode.

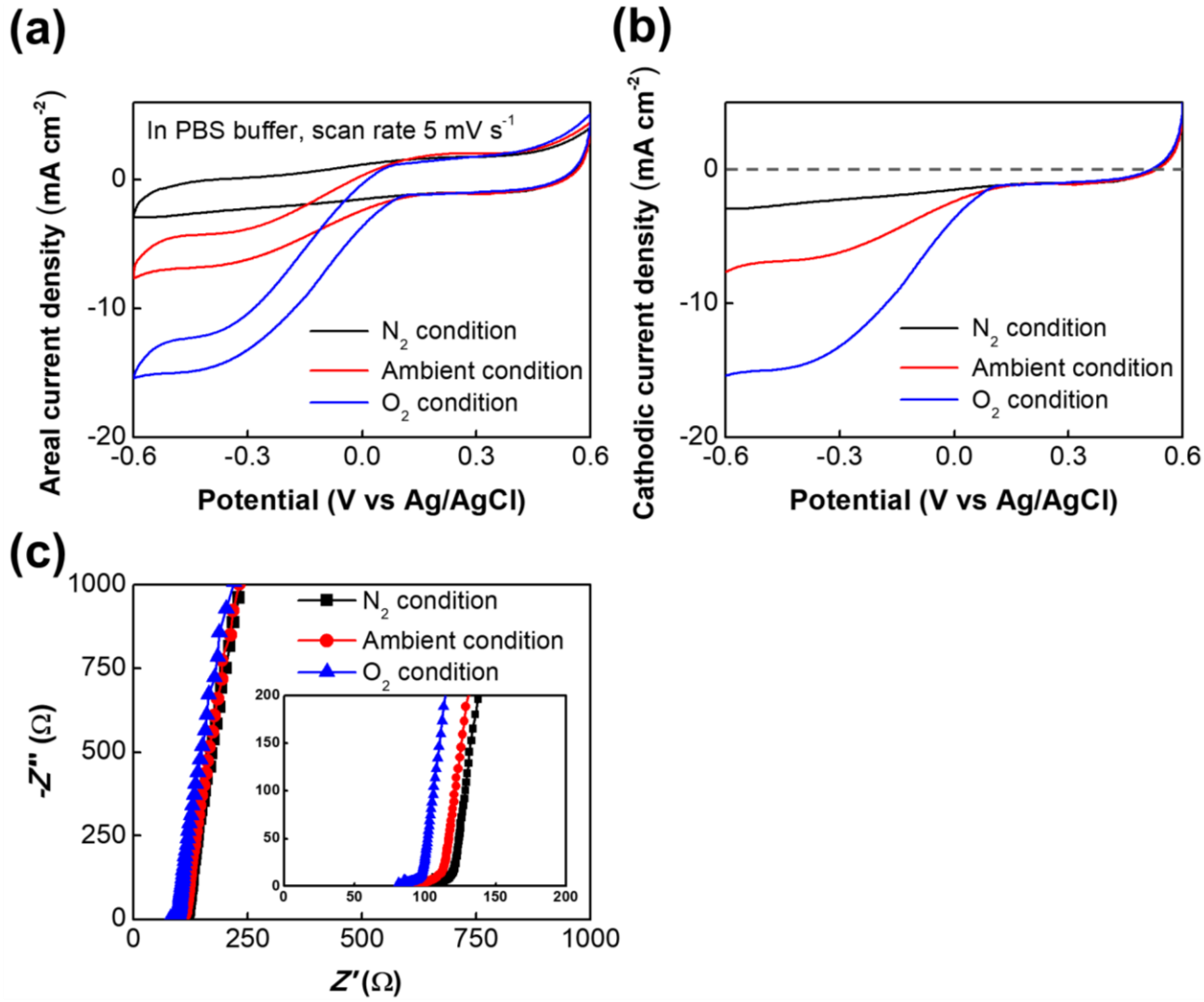

Fig. S9 Electrochemical performance of 20-Au-CF. (a) Cyclic voltammograms, (b) cathodic current density curves, and (c) Nyquist plots of 20-Au-CF in PBS buffer solution under N_2, ambient, and O_2 conditions. The ESR was 110, 100, and 88 Ω for N_2, ambient, and O_2 conditions, respectively.

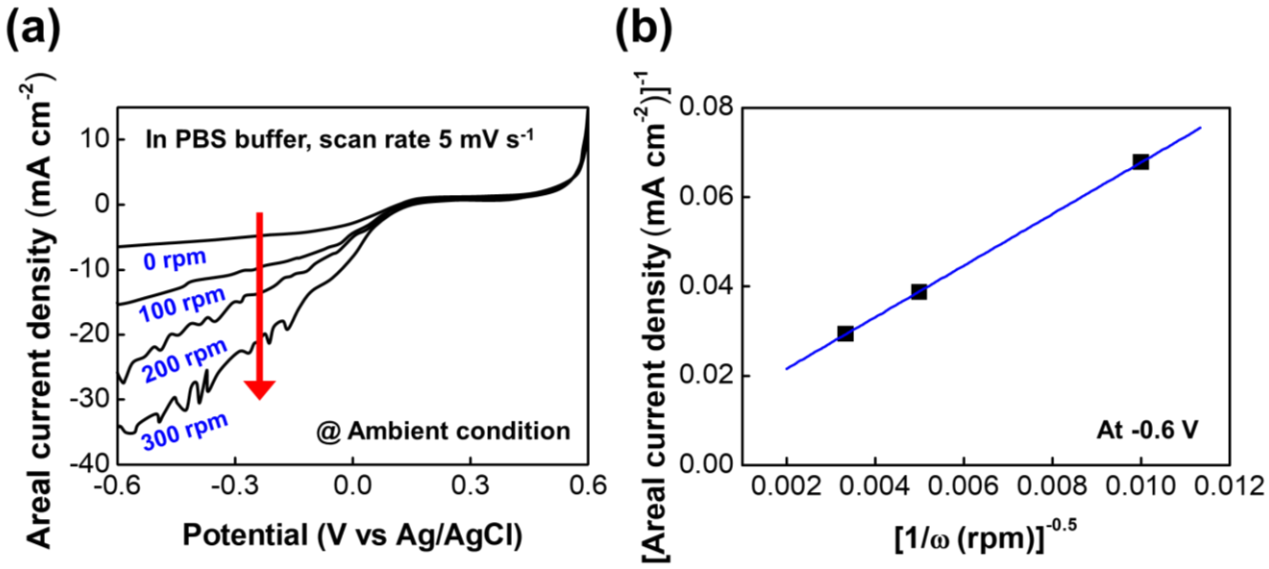

Fig. S10 ORR (oxygen reduction reaction) trend of Au-CF cathode as a function of the rotating speed of a stirring bar in a cell. (a) Current-potential curves at different rotation speeds in PBS buffer (20 mmol L^{-1} phosphate, 0.14 mol L^{-1} NaCl, pH 7.4) at a scan rate of 5 mV s^{-1} in ambient condition. (b) The relationship between the rotation speed and the areal current density of Au-CF cathode. ω is the revolution per minute.

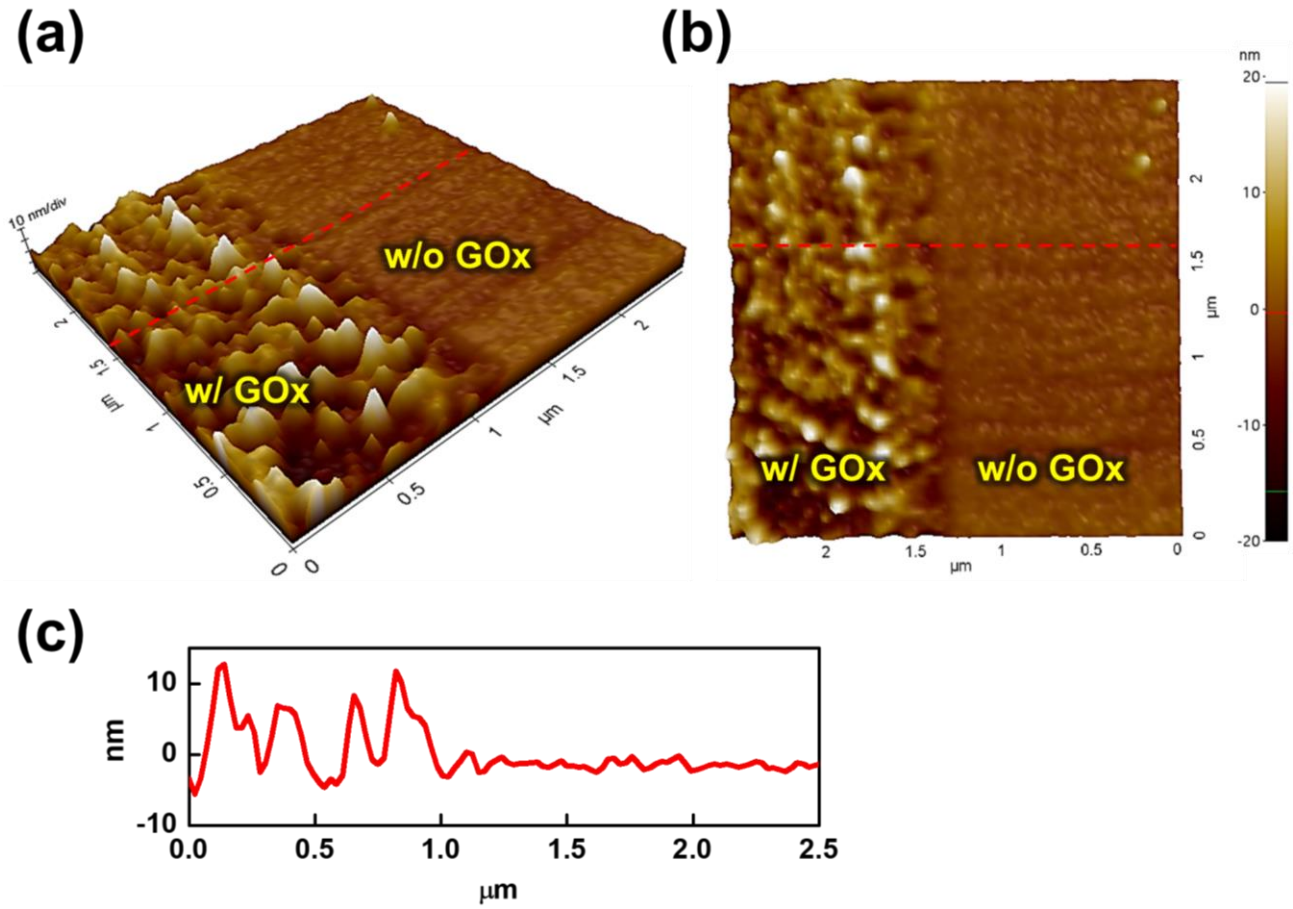

Figure S11. (a) Tilted and (b) top-view AFM images of the enzyme layer deposited on the Au substrate. (c) Line profile analysis obtained from the red dashed line of (a) and (b) images. The thickness of the enzyme layer [(GOx/TREN)$_{20}$] is measured to be approximately 10 nm (from the height profile between the bare Au substrate without GOx multilayers and the GOx multilayer-coated Au substrate).

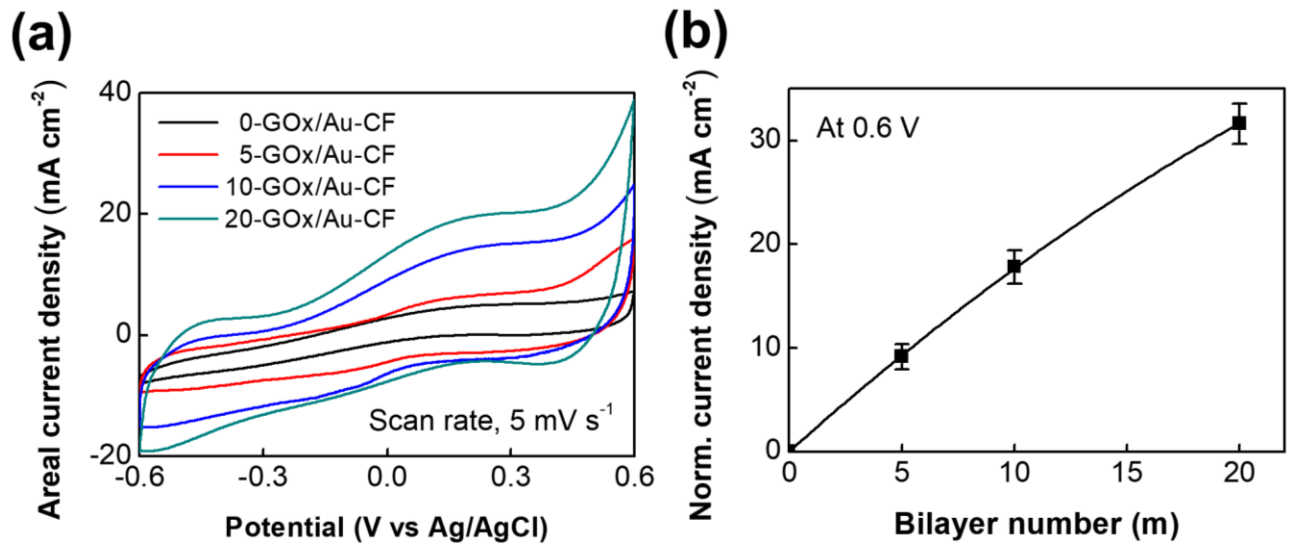

Fig. S12 (a) Cyclic voltammograms of the m-GOx/Au-CF anode with increasing number of (GOx/TREN) bilayers (m). All the measurements were performed at a scan rate of 5 mV s^{-1} in PBS under ambient conditions. (b) Normalized anodic current density levels at +0.6 V; here, the normalized level is defined as the current density level for which the anodic current density level of Au-CF (m=0) is subtracted from the anodic current density level of m-GOx/Au-CF at the specific potential of +0.6 V.

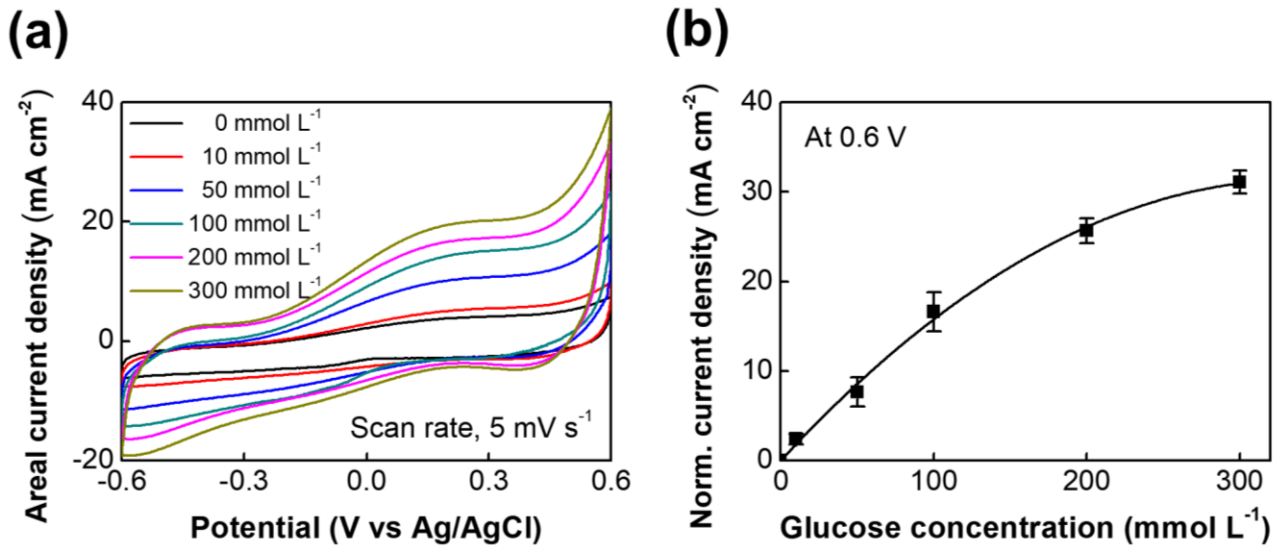

Fig. S13 Electrochemical performance of the anode (20-GOx/20-Au-CF). (a) Cyclic voltammograms as a function of glucose concentration. (b) Normalized anodic current density levels of the anode measured at +0.6 V as a function of glucose concentration.

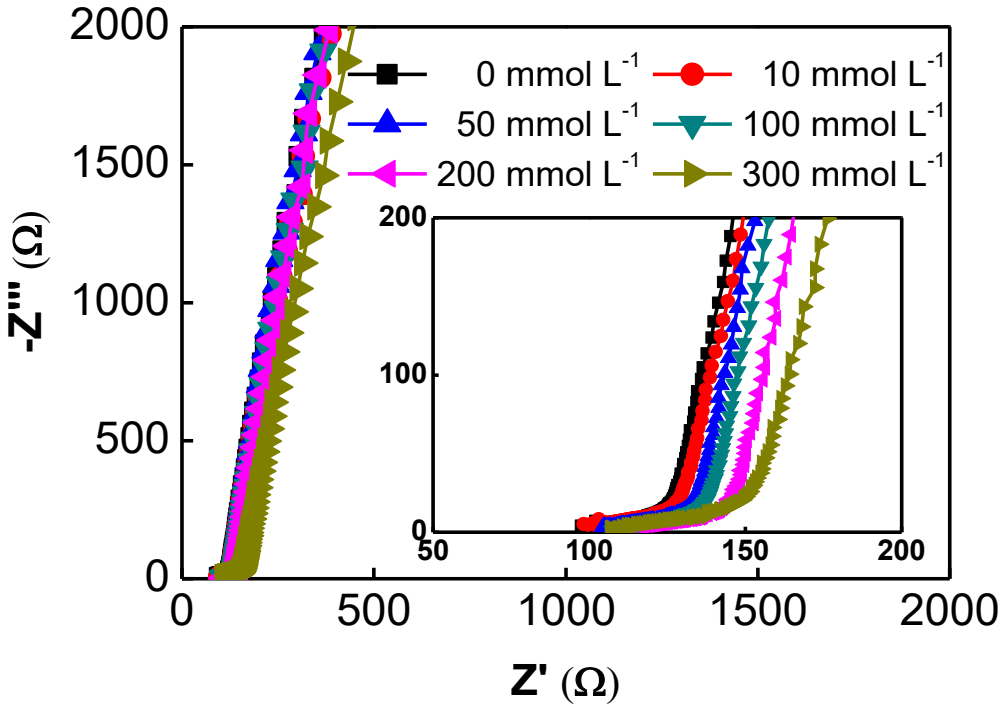

Fig. S14 Nyquist plots of the 20-GOx/20-Au-CF anode as a function of glucose concentration. The inset shows the high-frequency region. All the measurements were performed at a scan rate of 5 mV s^{-1} in a PBS under ambient conditions.

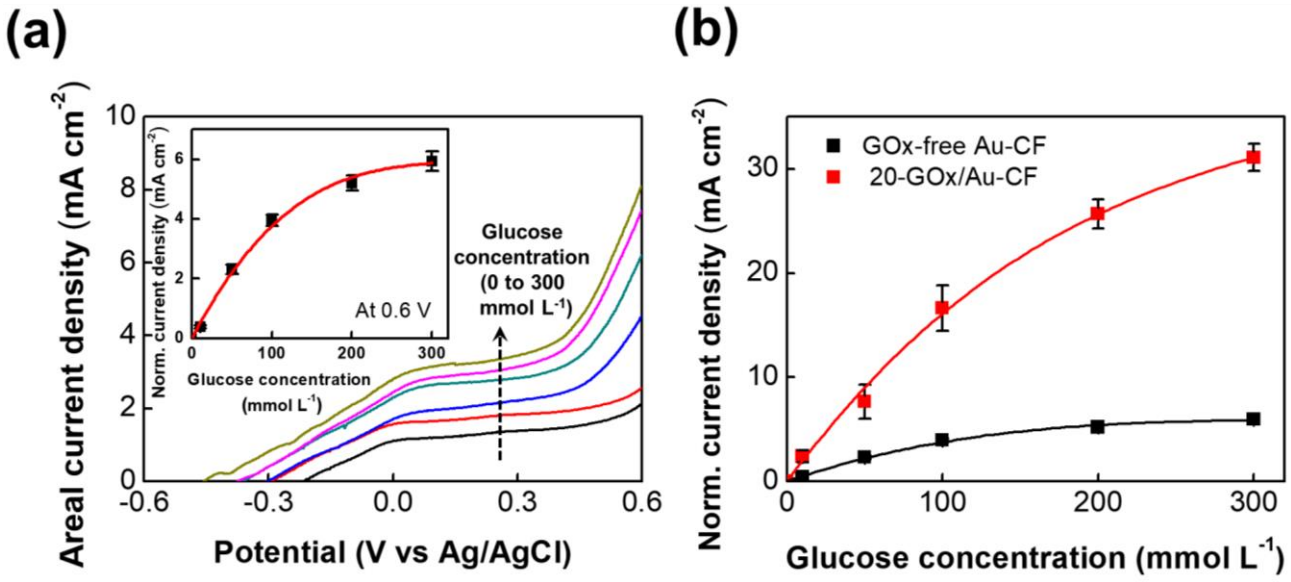

Fig. S15 GOx-free Au-CF anode. a, Electrooxidation of GOx-free Au-CF at the different glucose concentration of 10, 50, 100, 200, and 300 mmol L^{-1}, respectively. Inset indicates the normalized current density (in mA cm^{-2}) as a function of glucose concentration recorded at a potential of +0.6 V. **b**, Comparison of electrooxidation activities of GOx-free and 20-GOx/Au-CF anode electrodes at different glucose concentration. The electrochemical test was performed at a scan rate of 5 mV s^{-1} in a PBS (pH 7.4) under ambient condition. The normalized current density is obtained by subtracting the current density at +0.6 V measured in PBS without glucose. In this case, the oxidation of Au NPs loaded on the Au-CF electrode (~19%) was observed for GOx-free anode electrode.

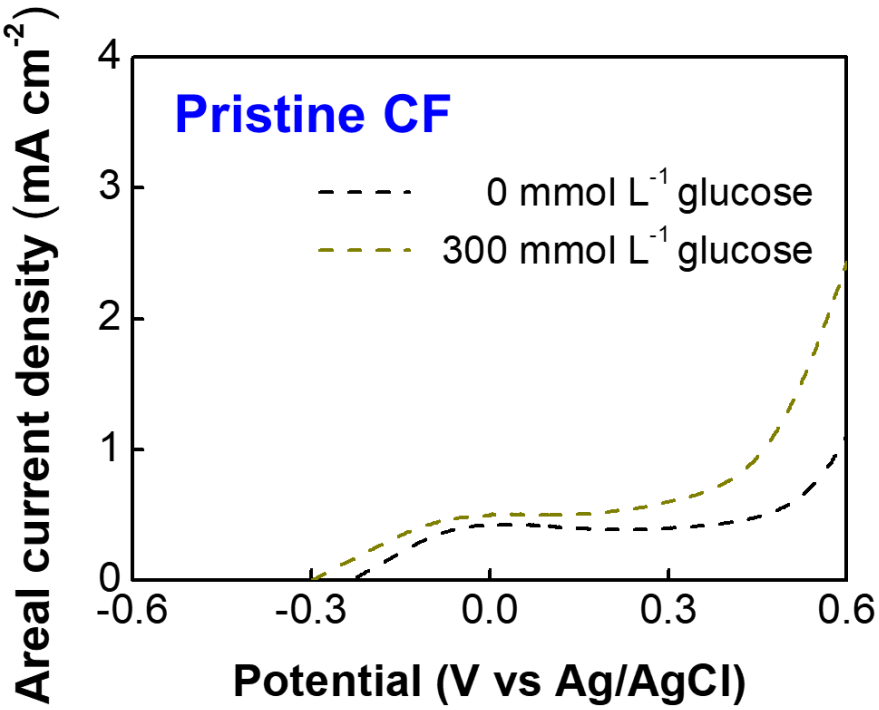

Fig. S16 Anodic current density performance in the absence of TOABr-Au NP/TREN layer on CF electrode. Polarization curves for oxidation reaction of the anode in 0 mmol L^{-1} (glucose-free) and 300 mmol L^{-1} glucose buffer.

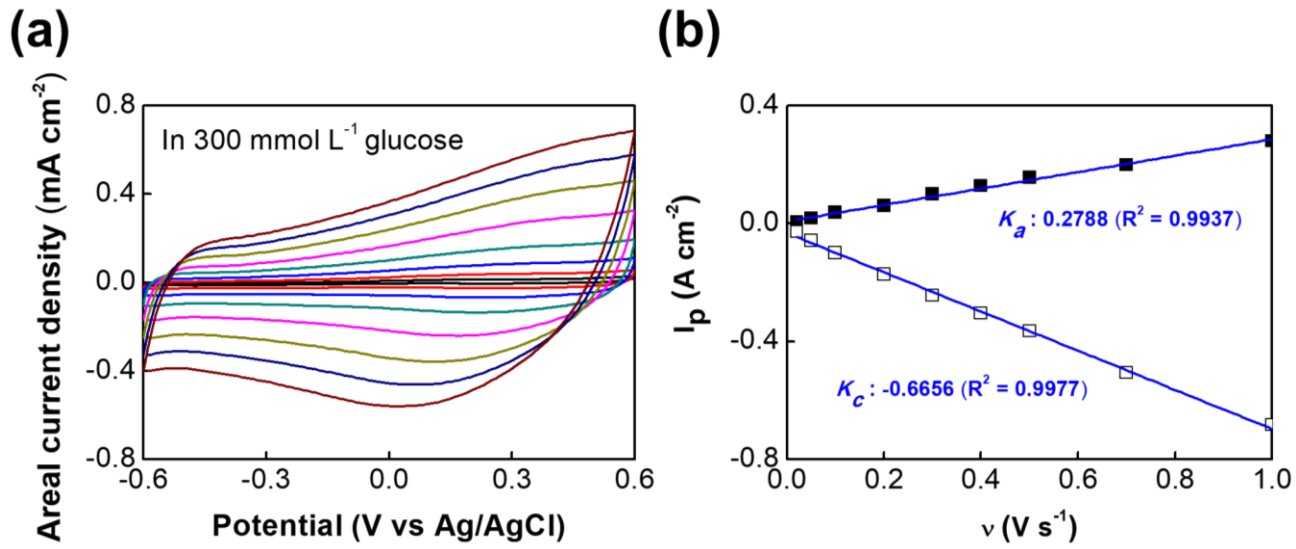

Fig. S17 Electrochemical response of the GOx-immobilized Au-CF anode. (a) Scan rate (ν)-dependent CVs of the anodic electrode, 20-GOx/Au-CF, in 300 mmol L^{-1} glucose buffer condition. Scan rates (from inner to outer of CV curves) were defined as 0.01, 0.02, 0.05, 0.1, 0.2, 0.3, 0.4, and 0.5 V s^{-1}. (b) The plot of the peak currents of 20-GOx/Au-CF as increasing the scan rate from 0.005 to 1 V s^{-1}. Linear dependence of anodic peak currents ($I_{p,a}$) and cathodic peak currents ($I_{p,c}$) on scan rates.

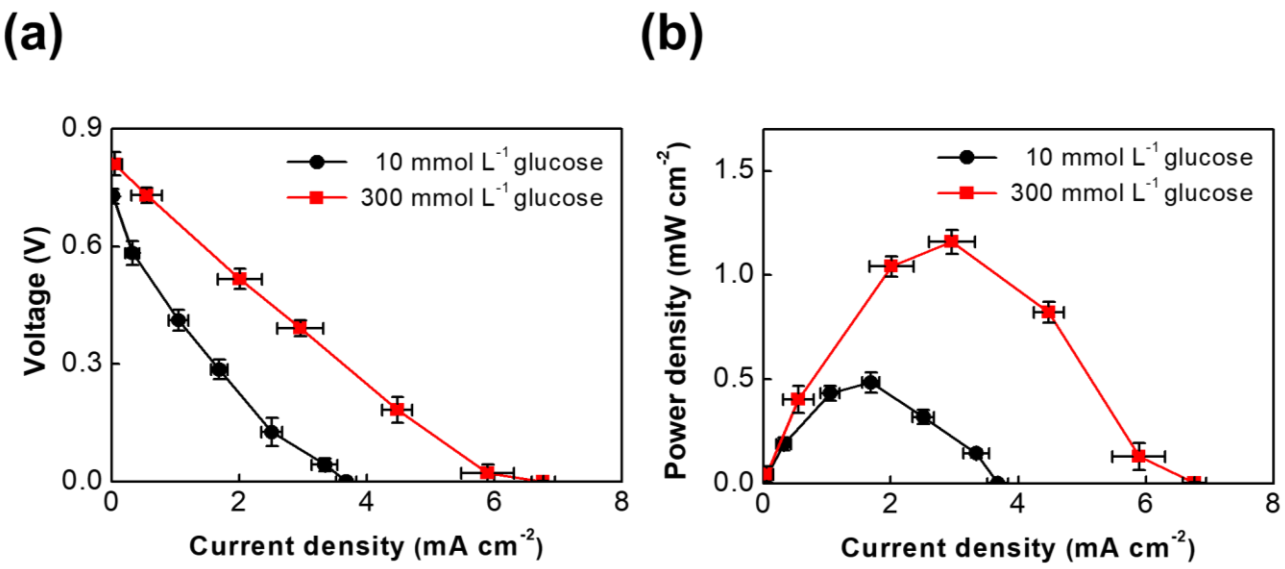

Fig. S18 Characteristics of Au-CF-BFCs. (a) The power density (*P*) – current (*I*) profiles of the hybrid Au-CF-BFC with different external resistances (1 kΩ – 10 MΩ). (b) The *V*–*I* profiles of the hybrid BFC with different external resistances (1 kΩ – 10 MΩ). All the measurements were performed in PBS containing glucose (10 mmol L^{-1} and 300 mmol L^{-1}) under ambient conditions at 37 °C. All error bars show the standard deviation from the mean value of power densities for three to five independent experiments.

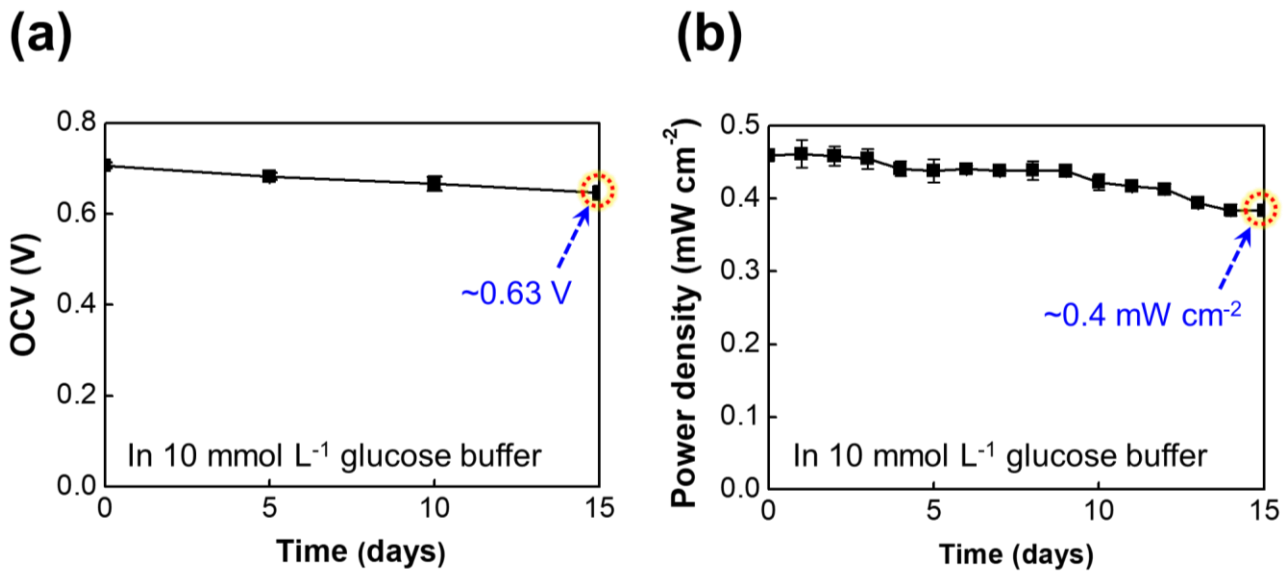

Fig. S19 (a) OCV changes, which is measured under open-circuit system, and (b) Power density changes of the complete hybrid Au-CF-BFC with external variable resistors, in 10 mmol L^{-1} glucose buffer for 15 days. All error bars show the standard deviation from the mean value of power densities for three to five independent experiments.

Table S1. Specific data sheet of $(GOx/TREN)_m$ multilayers.

m	Terminated with	ESR (Ω)	R_{et} [a] (Ω)
20	TREN	62.5	63
20.5	GOx	62.8	757
21	TREN	63.8	64
21.5	GOx	67.1	1415
22	TREN	66.1	66
22.5	GOx	66.8	1836
23	TREN	74.9	75

[a] The interfacial electron transfer resistance between the charged interface of the electrode and the electrolyte.

Table S2. Comparison of Au-CF-based glucose BFC performances based on the direct electron transfer, measuring power density under changing loads.

Electrode[a)]	Catalyst[b)]	Operation condition	P_{max} [mW cm^{-2}]	Stability	OCV[c)] [V]	Reference
Au-CF	**GOx/Au NP**	**PBS (pH 7.4) at 37º C, ambient**	**1.2**	**84% power after 15 days**	**0.81**	**This work**
Compressed MWCNT/enzyme composite	GOx/Lac	In the abdominal cavity of a rat	0.193	No signs of rejection or inflammation after 110 days	0.57	3
Graphene and SWCNT cogel	GOx/BOD	Air-saturated sodium phosphate buffer (0.1 M, pH 7.0) with 100 mM glucose	0.19	-	0.61	4
CS/CNC film (on glassy carbon)	GOx/Pt sheet	Air-saturated PBS (pH 7.2) containing 10 mM glucose	0.06	-	0.59	5
SWCNT (for anode) & PHE-CNT film (on glassy carbon) (for cathode)	GOx-Cat/ Lac	0.2 M phosphate buffer solution (pH 7.1) saturated with dioxygen and containing 0.21 M glucose.	0.04	~41% OCV after 15 days	0.4	6
Nafion nanowire (on Au electrode)	GOx/Lac	1 wt% glucose/PBS Solution (pH 7.0)	0.03	-	0.23	7
NAD(P)+-dependent SWCNT	GDH/BOD	0.1 M phosphate buffer solution (pH 7.0) with glucose 40 mM	0.023	-	~0.72	8
SWNT (on glassy carbon)	GDH/Lac	PBS (pH 6) at 20 ºC, ambient	0.0095	80% power after 1 day	0.8	9
10	CDH/Lac	0.1 M citrate–phosphate air-saturated buffer, pH 4.5	0.005	-	0.73	10

[a)] The abbreviations for different electrodes. Au-CF: Au NP-coated carbon fiber, $(TOABr\text{-}Au\ NP/TREN)_{20}$-coated carbon fiber, MWNT: multi-walled carbon nanotube, SWNT: single-walled carbon nanotube, CS/CNC: chitosan/carbon nanochips, PHE-CNT: Phenylation of SWNT on side walls, NAD(P)+: β-nicotinamide adenine dinucleotide-(NAD+) or β-nicotinamide adenine dinucleotide phosphate-(NADP+), SPGE: spectrographic graphite electrode. [b)] The abbreviations for different enzymes: glucose oxidase (GOx), laccase (Lac), bilirubin oxidase (BOD), glucose dehydrogenase (GDH), CDH (cellobiose dehydrogenase), and catalase (Cat). [c)] Open circuit voltage (OCV).

References

1 M. Ni, D. Y. C. Leung, M. K. H. Leung, *Int. J. Hydrogen Energ.*, 2007, **32**, 3238–3247.

2 A. R. Vancha, S. Govindaraju, K. V. L. Parsa, M. Jasti, M. González-García, R. P. Ballestero, *BMC Biotechnol.*, 2004, **4**, 1–12.

3 A. Zebda, S. Cosnier, J. -P. Alcaraz, M. Holzinger, A. LeGoff, C. Gondran, F. Boucher, F. Giroud, K. Gorgy, H. Lamraoui and P. Cinquin, *Sci. Rep.*, 2013, **3**, 1516.

4 A. S. Campbell, Y. J. Jeong, S. M. Geier, R. R. Koepsel, A. J. Russell, M. F. Islam, *ACS Appl. Mater. Interfaces*, 2015, **7**, 4056−4065.

5 Z. Kang, K. Jiao, C. Yu, J. Dong, R. Peng, Z. Hu, S. Jiao, *RSC Adv.*, 2017, **7**, 4572–4579.

6 K. Stolarczyk, D. Łyp, K. Żelechowsk, J. Biernat, F., J. Rogalski, R. Bilewicz, *Electrochim. Acta*, 2012, **79**, 74–81.

7 C. Pan, Y. Fang, H. Wu, M. Ahmad, Z. Luo, Q. Li, J. Zie, Z. Yan, L. Wu, Z. L. Wang, J. Zhu, *Adv. Mater.*, 2010, **22**, 5388–5392.

8 Y. -M. Yan, O. Yehezkeli, I. Willner, *Chem. Eur. J.*, 2007, **13**, 10168–10175.

9 Y. Yan, W. Zheng, L. Su, L. Mao, *Adv. Mater.*, 2006, **18**, 2639–2643.

10 V. Coman, C. Vaz-Domínguez, R. Ludwig, W. Harreither, D. Haltrich, A. L. De Lacey, T. Ruzgas, L. Gorton, S. Shleev, *Phys. Chem. Chem. Phys.*, 2008, **10**, 6093–6096.